Journal of Physics: Condensed Matter

Magnetic order of Nd_5Pb_3 single crystals

To cite this article before publication: Jiaqiang Yan *et al* 2018 *J. Phys.: Condens. Matter* in press https://doi.org/10.1088/1361-648X/aaaf3e

Magnetic order of Nd_5Pb_3 single crystals

J.-Q. Yan,[1,2,*] M. Ochi,[3] H. B. Cao,[4] B. Saparov,[5] J.-G. Cheng,[6]
Y. Uwatoko,[7] R. Arita,[8] B. C. Sales,[1] and D. G. Mandrus[1,2]

[1] *Materials Science and Technology Division, Oak Ridge National Laboratory, Oak Ridge, TN 37831, United States*
[2] *Department of Materials Science and Engineering, University of Tennessee, Knoxville, Tennessee 37996, United States*
[3] *Department of Physics, Osaka University, Toyonaka, Osaka 560-0043, Japan*
[4] *Quantum Condensed Matter Division, Oak Ridge National Laboratory, Oak Ridge, TN 37831, United States*
[5] *Department of Chemistry and Biochemistry, Stephenson Life Sciences Research Center, University of Oklahoma, Norman, OK 73019, United States*
[6] *Beijing National Laboratory for Condensed Matter Physics, and Institute of Physics, Chinese Academy of Sciences, Beijing 100190, P. R. China*
[7] *The Institute for Solid State Physics, The University of Tokyo, Kashiwa, Chiba 277-8581, Japan*
[8] *RIKEN Center for Emergent Matter Science, 2-1 Hirosawa, Wako, Saitama 351-0198, Japan*

(Dated: February 4, 2018)

We grow millimeter-sized Nd_5Pb_3 single crystals out of a Nd-Co flux. We experimentally study the magnetic order of Nd_5Pb_3 single crystals by measuring the anisotropic magnetic properties, electrical resistivity under high pressure up to 8 GPa, specific heat, and neutron single crystal diffraction. Two successive magnetic orders are observed at T_{N1}=44 K and T_{N2}=8 K. The magnetic cells can be described with a propagation vector k=(0.5,0,0). Cooling below T_{N1}, Nd1 and Nd3 order forming ferromagnetic stripes along the b-axis, and the ferromagnetic stripes are coupled antiferromagnetically along the a-axis for the k=(0.5,0,0) magnetic domain. Cooling below T_{N2}, Nd2 orders antiferromagnetically to nearby Nd3 ions. All ordered moments align along the crystallographic c-axis. The magnetic order at T_{N1} is accompanied by a quick drop of electrical resistivity upon cooling and a lambda-type anomaly in the temperature dependence of specific heat. At T_{N2}, no anomaly was observed in electrical resistivity but there is a weak feature in specific heat. The resistivity measurements under hydrostatic pressures up to 8 GPa suggest a possible phase transition around 6 GPa. Our first-principles band structure calculations show that Nd_5Pb_3 has the same electronic structure as does Y_5Si_3 which has been reported to be a one-dimensional electride with anionic electrons that do not belong to any atom. Our study suggests that R_5Pb_3 (R=rare earth) can be a materials playground for the study of magnetic electrides. This deserves further study after experimental confirmation of the presence of anionic electrons.

INTRODUCTION

The intermetallic compounds R_5Pb_3 (R=rare earth) crystallize in the Mn_5Si_3-typed hexagonal structure with the space group $P6_3/mcm$.[1] In this structure, the rare earth ions are located at two inequivalent crystallographic sites $R1$(4d) and $R2$(6g). Pb is located at the octahedral site (6g) only. As shown in Fig. 1, $R1$ stays inside of twisted trigonal prisms which share faces along c-axis forming a chain and share edges in the ab-plane forming a honeycomb array. $R2$ ions are arranged to form a chain of trigonal antiprisms and connected by sharing basal faces. One interesting feature of this structure is that the void in the center of each trigonal antiprism might host some small foreign ions without destabilizing the hexagonal structure.[2] This stuffing effect leads to a rich interstitial chemistry and affords a novel means of engineering band topology and thus physical properties of a given host. Complex magnetic phase transitions have been reported in R_5Pb_3 and Cu- or Ni-stuffed versions.[3–8] Compared to R_5M_3 (M=Si, Ge, Sn) where interesting magnetism, magnetoresistivity, and heavy fermion have been reported,[9–13] R_5Pb_3 family is less studied and all previous work was done on polycrystalline samples.

R_5Pb_3 attracts our attention also because of Hosono's work on Y_5Si_3 and Nb_5Ir_3 with the same Mn_5Si_3-type structure. [14, 15] Y_5Si_3 was confirmed experimentally and theoretically as a 1-dimensional electride with $0.79e^-$ in the void behaving like anions.[14] In the isostructural Nb_5Ir_3, replacing the localized anionic electrons in the voids with oxygen atoms is reported to tune the superconducting transition temperatures. With the same structure, R_5Pb_3 can be a new materials playground to investigate possible relation between the physical properties and the anionic electrons.

In this work, we report the first flux growth of Nd_5Pb_3 single crystals and a thorough investigation of the magnetic order of this compound. Long range magnetic orders are observed at T_{N1}=44 K and T_{N2}=8 K, respectively, by measuring the magnetization, electrical resistivity, and specific heat. Our neutron single crystal diffraction shows that the magnetic cells can be described with a propagation vector k=(0.5,0,0). We also perform first-principles band structure calculations which suggest that Nd_5Pb_3 has the same electronic structure as does Y_5Si_3. The intrinsic magnetic and transport properties reported in this study enable a reliable comparison be-

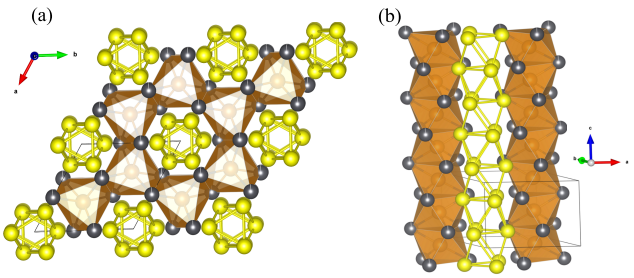

FIG. 1. (color online) A representation of the hexagonal structure of Nd_5Pb_3 viewed (a) down the c-axis, and (b) along c-axis. Nd1, Nd2 and Pb atoms are colored as brown, yellow and black spheres, respectively.

tween Nd_5Pb_3 and those stuffed versions to understand possible effects of the interstitial ions in the voids. The reported growth protocol can be applied for the growth of most R_5Pb_3 members which makes possible further studies of their anisotrpoic and intrinsic physical properties.

EXPERIMENTAL DETAILS

Nd_5Pb_3 single crystals were grown out of Nd-Co flux.[16] In a typical growth, the starting materials Nd (99.999%, Ames Laboratory), Co (99.999%, Alfa Aesar), and Pb (99.9999%, Alfa Aesar) were placed in a 2 ml alumina crucible with a molar ratio of 7:2:1. A catch crucible containing quartz wool was mounted on top of growth crucible and both were sealed in a silica ampoule under approximately 1/3 atmosphere of argon gas. The sealed ampoule was heated to 1100^{o}C, dwelled at 1100^{o}C for 2h, and then cooled to 850^{o}C over 50h. Once the furnace reached 850^{o}C, the excess flux was decanted from the crystals.

Room temperature X-ray powder diffraction patterns were collected on a X'Pert PRO MPD X-ray Powder Diffractometer using Ni-filtered Cu-K_α radiation. The phase identification was carried out employing X'Pert HighScore Plus software. The elemental analysis was performed using a Hitachi TM-3000 tabletop electron microscope equipped with a Bruker Quantax 70 energy dispersive x-ray (EDX) system.

Magnetic properties were measured with a Quantum Design (QD) Magnetic Property Measurement System in the temperature interval $1.8\,\mathrm{K} \leq \mathrm{T} \leq 320\,\mathrm{K}$. The temperature dependent specific heat and electrical transport data were collected using a 14 Tesla QD Physical Property Measurement System in the temperature range of $1.9\,\mathrm{K} \leq \mathrm{T} \leq 300\,\mathrm{K}$. The temperature dependence of electrical resistivity under hydrostatic pressures up to 8 GPa was measured using the standard four-probe method in a cubic-anvil-type apparatus.[17]

Single crystal X-ray diffraction measurements were carried out with the aid of a Bruker SMART APEX CCD-based single crystal X-ray diffractometer. A hexagonal needle-shaped crystal was selected under a microscope and cut into suitable dimensions ($\approx 0.082\times0.076\times0.070\,\mathrm{mm}^3$) inside Paratone N oil. The X-ray intensity data were acquired at 173(2) K with Mo Kα ($\lambda = 0.71073$ Å) radiation. Data collection, integration, and semi-empirical absorption correction based on equivalents were performed using SMART, SAINT and SADABS, respectively, all within the SHELXTL package. The structure refinement was carried out using the SHELXTL software package. Site occupation factors (SOF) were checked by freeing individual occupancies of atom sites.

Single crystal neutron diffraction was measured at HB-3A four-circle diffractometer at the High Flux Isotope Reactor at the Oak Ridge National Laboratory. A neutron wavelength of 1.546 Å was used with a bent perfect Si-220 monochromator.[18] The data were refined by the Rietveld method using Fullprof.[19]

RESULTS

Crystal growth and characterization

As described before,[16] the alumina crucible can oxidize some Nd leading to the growth of Nd_5Pb_3O crystals. We noticed that a shorter dwelling time at the homogenizing temperature and a faster cooling rate favor the growth of Nd_5Pb_3. Both factors reduce the amount of oxidization and hence the oxygen content in the melt. As shown in inset of Fig. 2, Nd_5Pb_3 crystals are normally about 2-3 mm long with a hexagonal cross section, which is different from the rectangular cross section of Nd_5Pb_3O crystals. Elemental analysis confirmed the atomic ratio and did not see any signal from Co. This confirms that Co is one important component in the flux to lower the melting temperature of the melt but does not contaminate the desired crystals.[16] The room temperature X-ray powder diffraction pattern can be indexed with hexagonal $P6_3/mcm$ symmetry. As highlighted by the star, there are two extra reflections from residual lead flux on crystal surface. This residual flux on the crystal surface leads to zero electrical resistivity observed in some resistivity measurements below 7 K when Pb superconducts.

Nd_5Pb_3O has a tetragonal structure (space group $I4/mcm$). There is no report whether a critical amount of O content, x_c, is needed in $Nd_5Pb_3O_x$ to induce the lattice symmetry change from the hexagonal $P6_3/mcm$ to the tetragonal $I4/mcm$. To confirm our crystals are oxygen free Nd_5Pb_3 instead of hexagonal $Nd_5Pb_3O_x$ with $x<x_c$, we performed single crystal X-ray and neutron diffraction studies. The structure refinement does not provide any evidence for the partial occupancy of oxygen

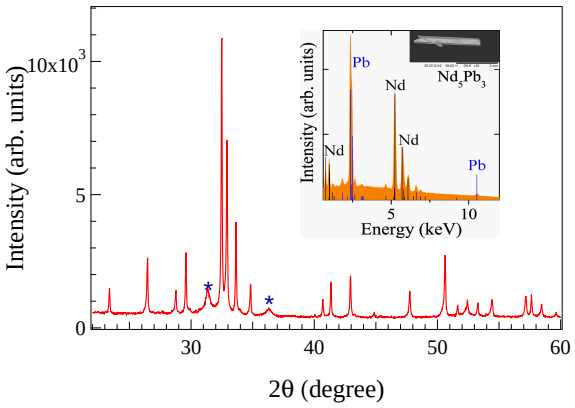

FIG. 2. (color online) Room temperature X-ray powder diffraction of pulverized single crystals. The ∗ symbol shows two peaks from lead flux on crystal surface. Inset shows the crystal picture and the EDX spectrum showing possible elements in the crystals.

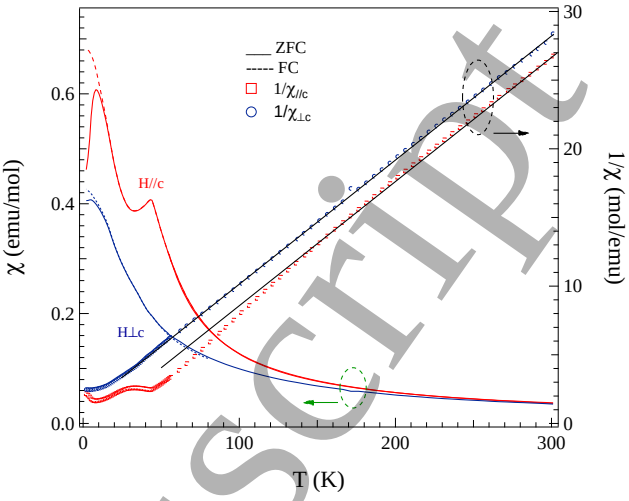

FIG. 3. (color online) Temperature dependence of magnetic susceptibility and inverse magnetic susceptibility measured in a magnetic field of 10 kOe applied parallel and perpendicular to the crystallographic c-axis, respectively.

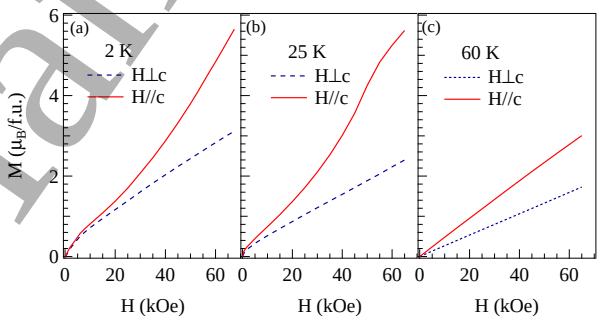

FIG. 4. (color online) Field dependence of magnetization at different temperatures: 2 K<T_{N2}, T_{N2}<25 K<T_{N1}, and T_{N1}<60 K.

in the voids of Nd trigonal antiprisms. Table 1 shows the refined structure parameters from X-ray single crystal diffraction at 173 K. Partial occupation of the voids by oxygen does not improve the refinement. The absence of oxygen is further confirmed by neutron single crystal diffraction which can better resolve the oxygen occupation.

Magnetic properties

Figure 3 shows the temperature dependence of magnetic susceptibility in a magnetic field of 10 kOe applied parallel and perpendicular to the crystallographic c-axis. The magnetic susceptibility curves measured in zero-field-cooled (ZFC) mode show a cusp around 8 K, and the ZFC and field-cooled (FC) curves split at ∼15 K. Above ∼20 K, the magnetic susceptibility measured with H⊥c, $\chi_\perp$, shows a Curie-Weiss-like temperature dependence. This is highlighted by the linear temperature dependence of $1/\chi_\perp$. In contrast, one cusp is observed around 44 K in the magnetic susceptibility measured with H∥c, $\chi_\parallel$. The plot of $1/\chi_\parallel$ suggests that $1/\chi_\parallel$ deviates from the high temperature linear fitting below ∼160 K. The linear fitting of $1/\chi_\perp$ in the temperature range 50 K≤T≤300 K yields an effective moment of 4.20 μ_B/Nd, and a Weiss constant of -12 K. Due to the slope change around 160 K, the linear fitting of $1/\chi_\parallel$ was performed in two different temperature intervals. The fitting in the temperature range 190 K≤T≤300 K yields an effective moment of 4.24 μ_B/Nd, and a Weiss constant of -0.3 K. The fitting of the low temperature data in the temperature range 50 K≤T≤150 K yields an effective moment of 3.92 μ_B/Nd, and a Weiss constant of 24 K. The obtained effective moments are a little larger than the expected 3.62 μ_B/Nd for Nd^{3+} ions. The temperature dependence of magnetic susceptibility suggests two magnetic transitions at T_{N1}=44 K and T_{N2}=8 K, respectively. The data also suggest that antiferromagnetic order is established below T_{N1} and a weak ferromagnetic component appears below T_{N2}. The magnetic ordering temperatures are further confirmed by specific heat, electrical resistivity, and neutron single crystal diffraction presented below.

Figure 4 shows the field dependence of magnetization at three different temperatures. At 60 K, magnetization shows a linear field dependence for both H⊥c and H∥c. At 25 K, a metamagnetic transition was observed around 40 kOe for H∥c, while it is absent for H⊥c. This suggests that an antiferromagnetic magnetic order occurs between 25K and 60 K and the magnetic moment is along the crystallographic c-axis. At 2 K, the magnetization curves show similar anisotropic field dependence as at 25 K. In addition to the metamagnetic transition, the magnetization curves at 2 K and 25 K show a ferro-

TABLE I. Structure parameters for Nd_5Pb_3 with the space group $P6_3/mcm$ (no. 193) at 173 K. Lattice parameters were determined to be a=9.2275(9)Å and c=6.7407(13)Å. The equivalent isotropic displacement parameter U_{eq} is defined as one third of the trace of the orthogonalized U_{ij} tensor.

atom	site	x	y	z	U_{eq}(Å^2)
Nd1	4d	1/3	2/3	0	0.0274(4)
Nd2	6g	0.23130(12)	0	0.25	0.0303(4)
Pb	6g	0.60214(7)	0	0.25	0.0271(4)

magnetic component. Linear fits to the M(H) data for H>20 kOe were performed. The slope of the high field linear fits gives the intrinsic susceptibility, and the H = 0 Oe intercept gives the saturation magnetization of the ordered phases. Cooling from 25 K to 2 K, the intrinsic susceptibility increases from $3.383(7)\times10^{-5}$ μ_B/fu to $4.096(3)\times10^{-5}$ μ_B/fu, and the saturation magnetization increases from $0.195(3)\mu_B$/fu to $0.374(14)\mu_B$/fu. This is consistent with the observation of the cusp in ZFC χ(T) curves and the splitting between ZFC and FC χ(T) curves shown in Fig 3.

Specific heat

Figure 5(a) shows the temperature dependence of specific heat in the temperature range 1.90 K≤T≤200 K measured in magnetic fields applied perpendicular to the crystallographic c-axis. A lambda-type anomaly can be well-resolved with a maximum at 44 K, suggesting that long range magnetic order occurs at this temperature. The transition temperature inferred from specific heat is consistent with that determined from $\chi_{\parallel}$. The specific heat data were also collected in applied magnetic fields of 60 kOe and 120 kOe, respectively. The applied magnetic field reduces the magnitude of the lambda-type anomaly and shifts it to lower temperatures. This also supports the conclusion that an antiferromagnetic order occurs at T_{N1}=44 K. No obviously anomaly can be resolved around T_{N2} in teh temperature dependence of specific heat. However, as plotted in the upper inset of Fig. 5, the applied magnetic field changes the magnitude of Cp/T below T_{N2}=8 K.

To estimate the entropy change across the magnetic order, we scaled the specific heat of La_5Pb_3 and subtracted it from that of Nd_5Pb_3. Figure 5(b) shows the magnetic specific heat, ΔC_p, and the entropy change, S, obtained by integrating ΔC_p/T from 1.90 K to 200 K. In addition to the anomaly around T_{N1}=44 K, a weaker feature was observed below 20 K in the temperature dependence of ΔC_p. This weak anomaly peaks at about 10 K, which is close to T_{N2}=8 K determined from magnetic susceptibility curves shown in Fig. 3. The total entropy change is roughly 46 J/mol K, which is about half of the expected $5R\ln(2J+1)$=96J/mol K for Nd^{3+}. The entropy change

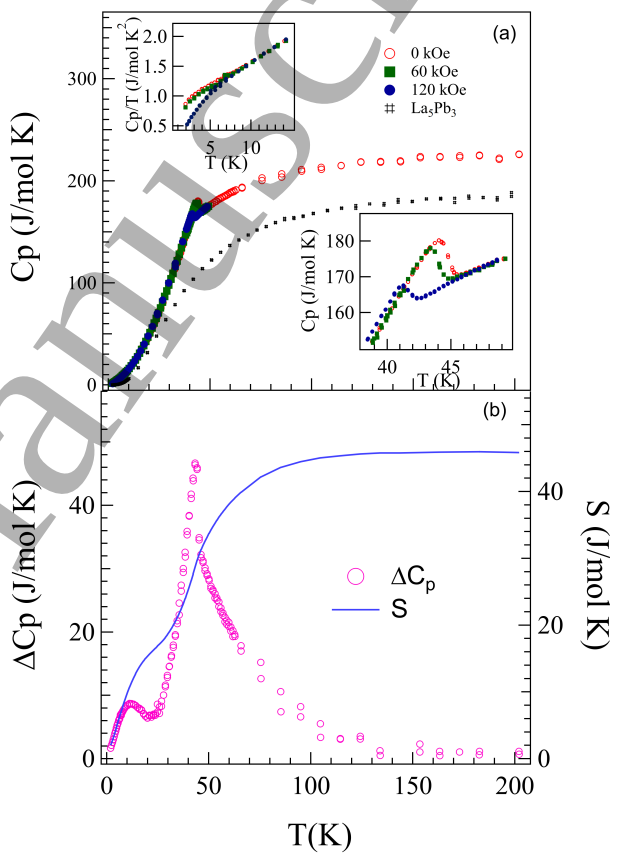

FIG. 5. (color online) (a) Temperature dependence of specific heat. Upper inset plots the temperature dependence of Cp/T highlighting the field effect around T_{N2}=8 K. Lower inset highlights the details around T_{N1} in three different magnetic fields. Also shown in this panel is the specific heat of La_5Pb_3, which is used as phonon reference. (b) The magnetic specific heat, ΔC_p, and the entropy change, S, across the transitions.

across T_N=44 K obtained by integrating between 15 K and 200 K is about 32 J/mol K.

Electrical resistivity

Figure 6 shows the temperature dependence of electrical resistivity measured with the electrical current par-

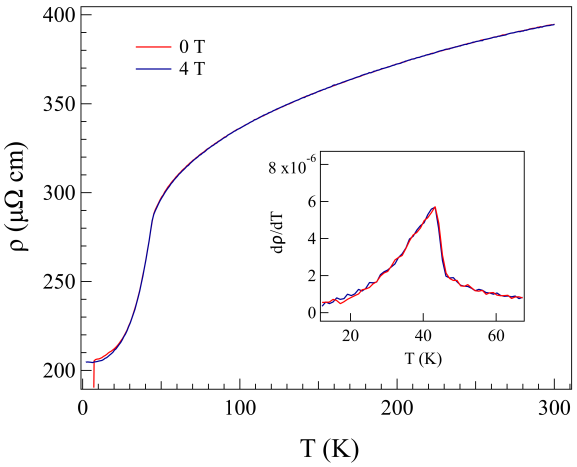

FIG. 6. (color online) Temperature dependence of the electrical resistivity measured with the electrical current parallel to the crystallographic c-axis. The magnetic field is applied perpendicular to the c-axis. Inset shows the derivative of the electrical resistivity around T_{N1}.

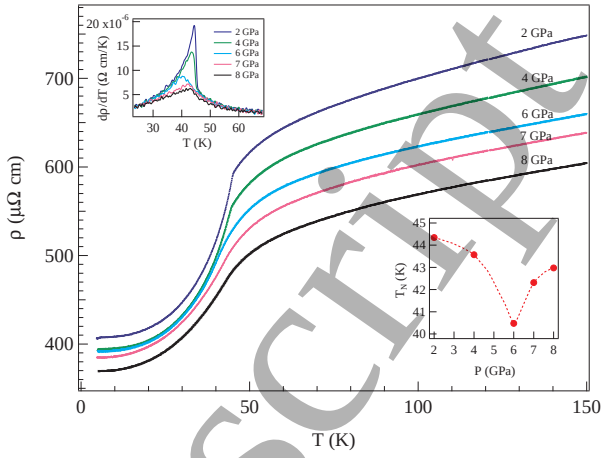

FIG. 7. (color online) Temperature dependence of the electrical resistivity under high pressure measured with the electrical current parallel to the crystallographic c-axis. The upper inset shows the derivative of the electrical resistivity. The lower inset shows the pressure dependence of T_{N1} and the dashed curve is a guide to the eyes.

allel to the crystallographic c-axis. Upon cooling, the electrical resistivity decreases from a room temperature value of $\sim$400 $\mu\Omega$.cm. A sharp drop of resistivity was observed across T_{N1}, which signals the significantly reduced effect of magnetic scattering on the electron transport. A sharp resistivity drop around 7 K is sometimes observed due to the filamentary superconductivity of lead flux on the crystal surface. This resistivity drop can be eliminated by applying an external magnetic field. Figure 6 also shows the temperature dependence of electrical resistivity measured in an applied magnetic field of 40 kOe. It's noteworthy that the magnetoresistive effect is negligible in this field. No anomaly around T_{N1}=8 K was observed.

Figure 7 shows the effect of hydrostatic pressure up to 8 GPa on the electrical resistivity. High pressure increases the electrical conductivity and broadens the resistivity drop around T_{N1}. The latter is highlighted by the derivative of electrical resistivity shown in the inset of Fig. 7. If we define the peak temperature as T_{N1}, the results suggest a possible pressure-induced phase transition around 6 GPa, which deserves further study. As shown in the inset of Fig. 7, T_{N1} decreases with increasing pressure below 6 GPa and then increases with further increasing pressure. As no anomaly could be observed at T_{N2} in our measurement, the pressure dependence of T_{N2} remains unknown.

Neutron single crystal diffraction

To confirm the magnetic order and to determine the low temperature magnetic structure, we performed a neutron single crystal diffraction study below room temperature. Figure 8 shows the evolution with temperature of the intensity of the (0.5 -1 0) reflection of one Nd_5Pb_3 single crystal. The evolution suggests two magnetic transitions at T_{N1}=36 K and T_{N2}=8 K. We noticed that T_{N1} varies slightly with samples, which might come from the air sensitivity. The intensity change around 8 K confirms the magnetic origin of the anomalies observed in the temperature dependence of magnetic susceptibility and specific heat.

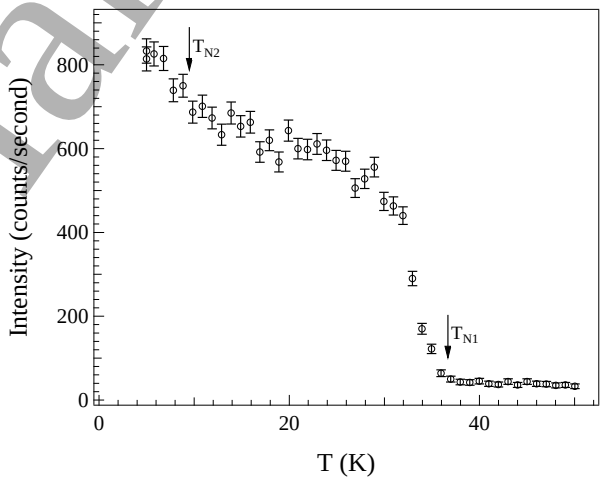

FIG. 8. (color online) Temperature dependence of the intensity of (0.5 -1 0) magnetic reflection.

In order to determine the detailed magnetic structure below T_{N1} and T_{N2}, we collected 90 magnetic reflections at 5 K and 25 K, respectively. The magnetic cell can be defined with a propagation vector k=(0.5, 0, 0). The best

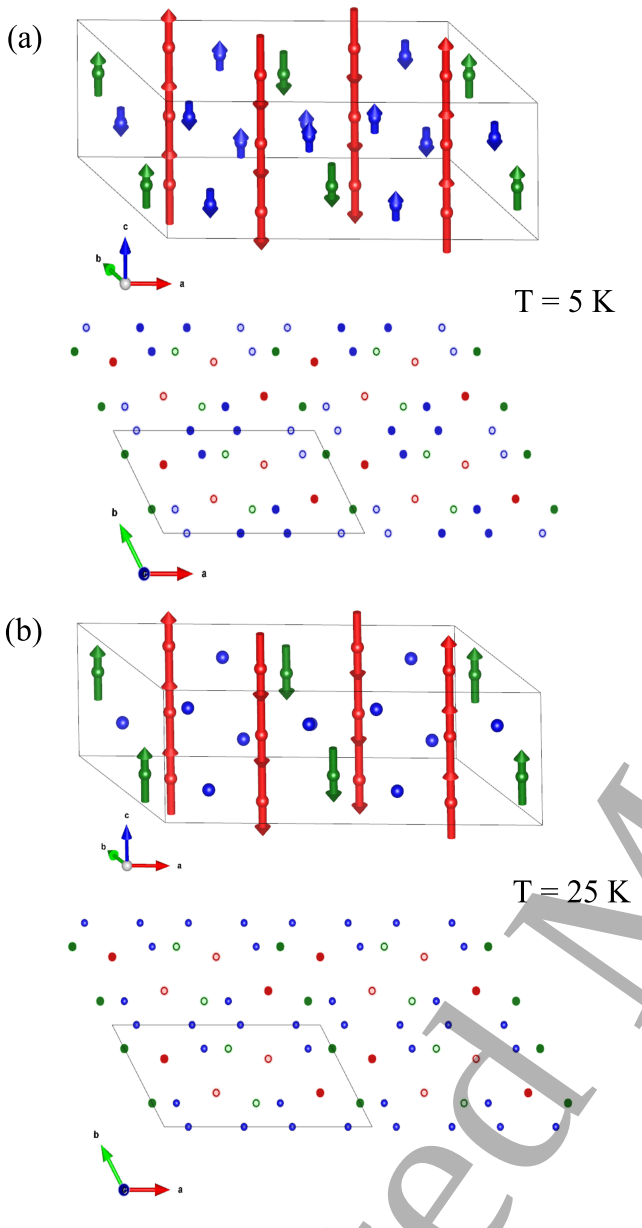

FIG. 9. (color online) Magnetic structure at (a) 5 K and (b) 25 K. Nd1, Nd2, and Nd3 are in red, blue, and green, respectively. Only Nd ions are shown for clarity. At 25 K, Nd2 ions are shown as solid circles but with zero moment.

fit magnetic symmetry is PBnma (62.454). [20] The in-plane magnetic component for the Nd1-site is symmetry allowed but does not improve the refinement. The refined in-plane magnetic moment within the error bar is zero. Therefore, the in-plane magnetic components are fixed to zero in the final refinement. To accommodate with the propagation vector in describing the magnetic structure, the Nd2 site splits to Nd2 (0.2310, 0, 1/4) and Nd3 (0, 0.2310, 1/4). The refined magnetic structures are plotted in Fig. 9. All Nd moments stay along the crystallographic c-axis. At 25 K, the Nd1 ions at 4d site order with a moment of 2.7(1)μ_B/Nd: the ferromagnetic chains couple antiferromagnetically along the a-axis. An ordered moment of 2.1(2)μ_B was observed on the Nd3 atoms which might be induced by the two ferromagneticlly aligned Nd1 ions nearby. The ordered moment is zero on the Nd2 sites, around which two Nd1 ions are coupled antiferromagnetically. As highlighted in Fig. 9, the ordering of the Nd1 and Nd3 sites form ferromagnetic stripes along the b-axis, and the ferromagnetic stripes are coupled antiferromagnetically along the a-axis for the k=(0.5,0,0) magnetic domain. Cooling below T_{N2}, all three Nd sites order with the same magnetic propagation vector. The ordered magnetic moments for Nd1, Nd2, and Nd3 are 3.2(1) μ_B, -1.1(1)μ_B, and 1.8(2)μ_B, respectively.

Band structure

To check possible anionc states in Nd_5Pb_3, we performed first-principles band structure calculations using the density functional theory (DFT) with the generalized gradient approximation (GGA) [21] and the full-potential linearized augmented plane-wave method as implemented in the WIEN2K code [22]. We also included $+U$ correction [23, 24] for Nd atoms with U = 9 eV. We assumed the experimental antiferromagnetic configuration, and the spin-orbit coupling was not included here for simplicity. The muffin-tin radii (RE) for Nd, Pb, and H atoms were 2.50, 2.50, and 1.79 Bohr, respectively. The maximum modulus for the reciprocal vectors $K_{\max}$ was chosen such that $REK\max$ = 8.0 and 5.5 for Nd_5Pb_3 and Nd_5Pb_3H, respectively. Note that the unit cell and the lattice vectors used in calculation are different from those shown in other parts of this paper.

Figure 10(a) and (b) show the calculated band structures of Nd_5Pb_3 and the virtual compound Nd_5Pb_3H where the hydrogen atoms were located at the same positions as those for Y_5Si_3H [25], respectively. By comparing their band structures, we can find a characteristic difference between them as indicated with black arrows. The Bloch states at the $(0, 0, \pi)$ point indicated with black arrows are shown in Fig. 10(c)-(d) for Nd_5Pb_3 and in Fig. 10(e)-(f) for Nd_5Pb_3H. As is evident in these figures, the extra bands in Nd_5Pb_3 can be regarded as the anion states extended in void space, which are rather localized around hydrogen atoms in Nd_5Pb_3H. This situation is the same as that found in Y_5Si_3 [14].

A sizable difference among the size of the spin magnetic moments on Nd atoms in our experiment was not reproduced by our first-principles calculations assuming the experimental antiferromagnetic configuration using the GGA+U+SOC method [23, 24] with U = 5 or 7 eV, which results in almost the same size of the spin magnetic moment on every Nd atom. This disagreement suggests that the complex magnetic structure observed in our experiment originates from some effects not included in our

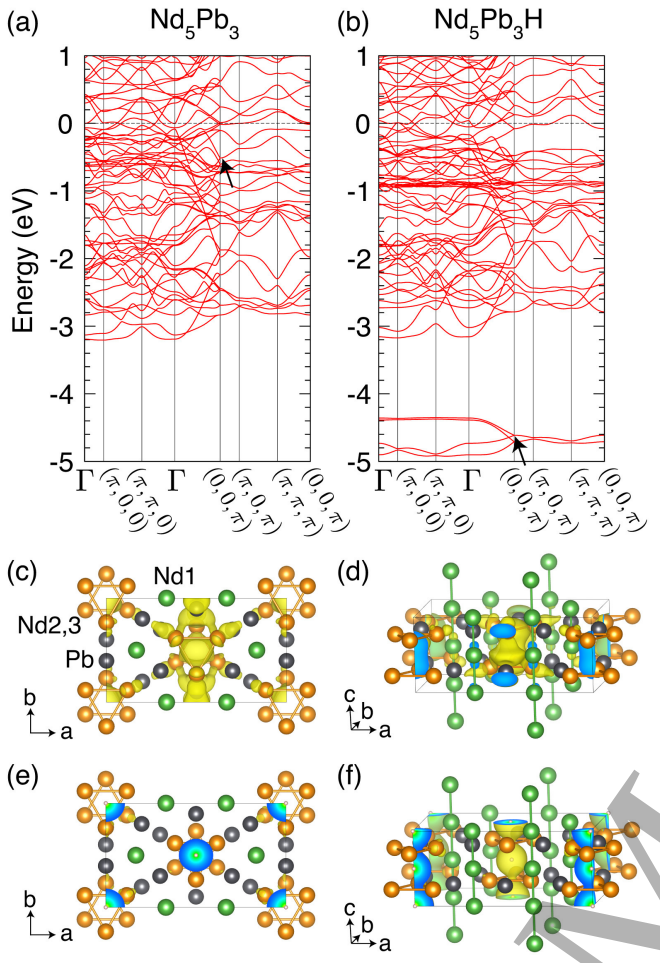

FIG. 10. (Color online) Band structures of (a) Nd_5Pb_3 and (b) Nd_5Pb_3H. The Fermi level is set to zero for each panel. Bloch states indicated with black arrows in (a) and (b) are drawn in (c)-(d) and in (e)-(f), respectively, using the VESTA software [26].

simple band structure calculations, such as the strong correlation effects for f-electrons or the spin frustration effect for the triangle network among Nd2 atoms.

DISCUSSION

Our measurements of magnetic properties, electrical resistivity, and specific heat suggest two successive magnetic phase transitions at T_{N1}=44 K and T_{N2}=8 K. Cooling from 25 K to 5 K, the ordered magnetic moment of Nd1 ions increases slightly from 2.7(1)μ_B to 3.2(1)μ_B, which is the same as the free ion value of gJ=3.27μ_B. This indicates that Nd1 is rather localized. In contrast, the ordered magnetic moments on Nd2(0.2310,0,1/4) and Nd3 (0, 0.2310, 1/4) ions are much smaller. The moment variation reflects the effect of different crystal electric fields at different crystallographic sites. Spin frustration effect from the triangle network among Nd2(0.2310,0,1/4) and Nd3 (0, 0.2310, 1/4) ions might also suppress the ordered moments on these two sites.

The results in Fig. 3 and 4 demonstrate that Nd_5Pb_3 shows anisotropic magnetic properties. This is consistent with the chain structure formed by the Nd1 and Nd2 ions. The slope change in $1/\chi_{\parallel}$ observed around 160 K is in contrast to the linear temperature dependence of $1/\chi_{\perp}$ in the paramagnetic state. It is worth mentioning that the Cuire-Weiss fitting of $1/\chi_{\perp}$ gives a nagative Weiss constant, suggesting dominant antiferromagnetic interactions. While the fitting of $1/\chi_{\parallel}$ below 160 K gives a positive constant suggesting dominant ferromagnetic interactions. The slope change of $1/\chi_{\parallel}$ around 160 K signals short range magnetic correlations below 160 K.

Neutron single crystal diffraction measurement suggests that both Nd2(0.2310,0,1/4) and Nd3 (0, 0.2310, 1/4) order in the temperature interval $T_{N2} \leq T \leq T_{N1}$, suggesting Nd-Nd exchange interactions in the two different Nd sites. This should be considered when understanding the effect on magnetic properties of high pressure or interstitial ions in the voids. The coincidence that the ordered Nd3 (0, 0.2310, 1/4) ions have two ferromagnetically aligned Nd1 neighbours indicate that the magnetic order at T_{N1} is driven by the ordering of Nd1 moments. With increasing pressure, the lattice contraction reduces the distance between magnetic Nd1 ions and nonmagnetic ligand ions which tends to weaken the localized electron magnetism. Above 6GPa, T_{N1} shows a positive pressure dependence. While pressure induced nuclear and/or magnetic phase changes are likely, those possible anionic electrons in the voids, once confirmed experomentally, should be considered in future studies. Under high pressure, the anionic electrons can interact with each other and also with nearly Nd ions affecting the magnetic interactions and even the magnetic ground states.[27]

Our DFT calculations of the band structure of Nd_5Pb_3 suggest extra bands from the anions states as in Y_5Si_3. Future experimental studies are needed to confirm the presence of anionic electrons in the voids of Nd_5Pb_3. However, the comparison between Nd_5Pb_3 and Nd_5NiPb_3 does not seem to suggest any obvious role of anionic electrons in determining the magnetic ordering temperatures. The magnetic and thermodynamic measurements on polycrystalline Nd_5NiPb_3 suggest two magnetic transitions: an antiferromagnetic transition at 42 K, and a weak-ferromagnetic canting transition at 8 K.[4] This similarity implies that filling the voids with nonmagnetic Ni does not affect the magnetic ordering of Nd ions.

SUMMARY

In summary, we report the first growth of Nd_5Pb_3 single crystals and this growth protocol works for most R_5Pb_3 members, which enables the study of the intrinsic and anisotropic properties of this family. We study the magnetic order in Nd_5Pb_3 single crystals by measuring magnetic and transport properties, specific heat, and neutron single crystal diffraction. Two successive magnetic orders take place at T_{N1}=44 K and T_{N2}=8 K. The magnetic cells can be described with a propagation vector k=(0.5,0,0). Cooling below T_{N1}, Nd1 and Nd3 order forming ferromagnetic stripes along b-axis, and the ferromagnetic stripes are coupled antiferromagnetically along a-axis. The coincidence that two nearest Nd1 ions around Nd3 are ferromagnetically aligned and those two around Nd2 are antiferromagnetically coupled suggests that the magnetic orderings of Nd ions at different sublattice are coupled. Below T_{N2}, Nd2 orders antiferromagnetically to nearby Nd3 ions. The temperature-dependent electrical resistivity shows a quick drop upon cooling below T_{N1} but no anomaly around T_{N2}. This suggests little effect on electrical transport from the Nd ions forming the trigonal antiprisms that can host anionic electrons. Band structure calculations show that the anionic states form the band dispersions near the Fermi level, which is similar to the case of Y_5Si_3. Future experimental studies are needed to confirm the presence of anionic electrons in the voids and its possible relation with the pressure dependence of T_{N1} above 6GPa. Comparison between Nd_5Pb_3 and Nd_5NiPb_3 suggests that filling the confined space in the trigonal antiprisms with nonmagnetic Ni does not affect the magnetic properties.

ACKNOWLEDGMENTS

Work at ORNL was supported by the U.S. Department of Energy, Office of Science, Basic Energy Sciences, Division of Materials Sciences and Engineering. The neutron diffraction work at ORNL was sponsored by the U.S. Department of Energy, Office of Science, Basic Energy Sciences, Scientific User Facilities Division. J.G.C. is supported by the National Science Foundation of China (Grant No. 11574377), the National Basic Research Program of China (Grant No.2014CB921500), the Strategic Priority Research Program and Key Research Program of Frontier Sciences of the Chinese Academy of Sciences (Grant Nos. XDB07020100, QYZDB-SSW-SLH013).

REFERENCES

* yanj@ornl.gov

[1] W. Jeitschko and E. Parthé, Acta Crystallographica **22**, 551 (1967).
[2] J. D. Corbett, E. Garcia, A. M. Guloy, W.-M. Hurng, Y.-U. Kwon, and E. A. Leon-Escamilla, Chemistry of Materials **10**, 2824 (1998).
[3] V. Tran, M. Gamża, A. Ślebarski, J. Jarmulska, and W. Miiller, Journal of Solid State Chemistry **180**, 2756 (2007).
[4] V. Goruganti, K. Rathnayaka, and J. H. Ross Jr, Journal of Applied Physics **105**, 07E118 (2009).
[5] V. Tran, J. Jarmulska, and W. Miiller, From the Coordinator of the national Scientific Network MAG-EL-MAT **25**, 327 (2007).
[6] V. Tran and L. Gulay, Journal of Solid State Chemistry **179**, 646 (2006).
[7] A. Marcinkova, C. de la Cruz, J. Yip, L. L. Zhao, J. K. Wang, E. Svanidze, and E. Morosan, Journal of Magnetism and Magnetic Materials **384**, 192 (2015).
[8] K. Sasao, R. Yamauchi, and K. Fukamichi, Journal of the Magnetics Society of Japan **23**, 489 (1999).
[9] K. Mukherjee, K. K. Iyer, and E. Sampathkumaran, Journal of Physics: Condensed Matter **23**, 066003 (2011).
[10] B. Maji, K. Suresh, and A. Nigam, EPL (Europhysics Letters) **91**, 37007 (2010).
[11] A. Tanaka, T. Tsutaoka, and T. Tokunaga, Journal of alloys and compounds **408**, 184 (2006).
[12] N. Mohapatra, K. Mukherjee, K. K. Iyer, and E. Sampathkumaran, Journal of Physics: Condensed Matter **23**, 496001 (2011).
[13] J. Lawrence, M. Hundley, J. Thompson, G. Kwei, and Z. Fisk, Physical Review B **43**, 11057 (1991).
[14] Y. Lu, J. Li, T. Tada, Y. Toda, S. Ueda, T. Yokoyama, M. Kitano, and H. Hosono, J. Am. Chem. Soc **138**, 3970 (2016).
[15] Y. Zhang, B. Wang, Z. Xiao, Y. Lu, T. Kamiya, Y. Uwatoko, H. Kageyama, and H. Hosono, npj Quantum Materials **2**, 45 (2017).
[16] J.-Q. Yan, Journal of Crystal Growth **416**, 62 (2015).
[17] J.-G. Cheng, K. Matsubayashi, S. Nagasaki, A. Hisada, T. Hirayama, M. Hedo, H. Kagi, and Y. Uwatoko, Review of Scientific Instruments **85**, 093907 (2014).
[18] B. C. Chakoumakos, H. Cao, F. Ye, A. D. Stoica, M. Popovici, M. Sundaram, W. Zhou, J. S. Hicks, G. W. Lynn, and R. A. Riedel, Journal of Applied Crystallography **44**, 655 (2011).
[19] J. Rodríguez-Carvajal, Physica B: Condensed Matter **192**, 55 (1993).
[20] S. V. Gallego, E. S. Tasci, G. Flor, J. M. Perez-Mato, and M. I. Aroyo, Journal of Applied Crystallography **45**, 1236 (2012).
[21] J. Perdew, K. Burke, and M. Ernzerhof, Errata:(1997) Phys Rev Lett **78**, 1396 (1996).
[22] P. Blaha, K. Schwarz, G. Madsen, D. Kvasnicka, and J. Luitz, An augmented plane wave+ local orbitals program for calculating crystal properties (2001).

[23] A. Liechtenstein, V. Anisimov, and J. Zaanen, Physical Review B **52**, R5467 (1995).
[24] S. Dudarev, G. Botton, S. Savrasov, C. Humphreys, and A. Sutton, Physical Review B **57**, 1505 (1998).
[25] I. MCCOLM, V. KOTROCZO, T. BUTTON, N. CLARK, and B. BRUER, Chemischer Informationsdienst **17** (1986).
[26] K. Momma and F. Izumi, Journal of Applied Crystallography **44**, 1272 (2011).
[27] M.-s. Miao and R. Hoffmann, Journal of the American Chemical Society **137**, 3631 (2015).